https://doi.org/10.5194/essd-2026-467
Preprint. Discussion started: 11 August 2026

Open Access Earth System Science Data Discussions

A 30-Year 1-km Daily Precipitation and Air Temperature Dataset for the Po River District (Italy)

Hossein Salehi[1,2], Daniele Andreis[2,3], Sohaib Baig[4], Gaia Roati[2,5], Marco Brian[5], Francesco Tornatore[5], Giuseppe Formetta[6], and Riccardo Rigon[2,6]

[1]Department of Physics, University of Trento, Trento, Italy
[2]Center Agriculture, Food and Environment (C3A), University of Trento, Trento, Italy
[3]Technology Transfer Centre, Fondazione Edmund Mach (FEM), San Michele all'Adige, Trento, Italy
[4]School of Geosciences, University of Edinburgh, Edinburgh, Scotland
[5]Po River Basin District Authority, Parma, Italy
[6]Department of Civil, Environmental and Mechanical Engineering, University of Trento, Trento, Italy

Correspondence: Gaia Roati (gaia.roati@adbpo.it)

Abstract.

High-resolution daily climate data remain scarce for complex Alpine terrain, where coarse gridded products often fail to resolve orographic precipitation gradients and elevation-dependent temperature variability. Here we present a 1-km gridded daily precipitation and temperature dataset for the Po River District (Northern Italy) covering the 1991–2020 climatological period. The dataset is based on a harmonized multi-source observational network comprising 1,583 precipitation and 1,555 temperature stations after quality control. Spatial interpolation was performed using Ordinary Kriging for precipitation and Detrended Kriging for temperature, with elevation as the trend variable, and daily-adaptive semivariogram models selected from five candidate functions via Particle Swarm Optimisation. Leave-one-out cross-validation indicates strong overall performance. For precipitation, the mean Kling–Gupta Efficiency (KGE) across all station-wise leave-one-out cross-validations exceeds 0.84 under All-Days conditions and 0.82 under Wet-Days conditions, with mean absolute errors of 1.28 mm and 3.05 mm, respectively. Temperature interpolation achieves a mean KGE of 0.88 and a mean absolute error of 1.14 °C, with negligible bias. Spatial diagnostics reveal higher precipitation errors in high-relief Alpine sectors and along basin boundaries, while temperature performance remains comparatively uniform. Interpolation skill decreases with altitude, particularly for precipitation during wet events, due to decreasing station density. The resulting dataset provides spatially continuous daily climate fields suitable for hydrological modelling, climate variability assessment, and environmental analysis in one of Europe's most topographically diverse river basins.

1 Introduction

High-resolution climate datasets are essential for hydrological modelling, environmental monitoring, agricultural management, and assessing earth observation products. Daily precipitation and temperature records are particularly important in regions characterised by strong topographic gradients, where short-term variability and elevation-dependent processes dominate hydroclimatic

https://doi.org/10.5194/essd-2026-467
Preprint. Discussion started: 11 August 2026

dynamics. In mountainous basins, coarse-resolution products may fail to resolve orographic precipitation patterns and temperature gradients, especially where elevation differences exceed several thousand metres (Hijmans et al., 2005; Aalto et al., 2013).

The Po River District (PRD) in northern Italy represents one of the most topographically diverse hydrological systems in Europe. Extending from sea level in the Adriatic delta to 4,800 m in the Alpine headwaters, the basin exhibits strong spatial contrasts in both precipitation and temperature (Zanchettin et al., 2008). These gradients influence snow accumulation, melt dynamics, runoff generation, and water resource availability across the region (Vezzoli et al., 2015).

Several widely used gridded datasets provide valuable climate information for Europe. However, none simultaneously combine (i) 1-km spatial resolution, (ii) daily temporal resolution, and (iii) continuous 30-year coverage (1991–2020) for the Po River District. WorldClim provides high-resolution climatological normals but lacks daily temporal resolution (Hijmans et al., 2005). TerraClimate offers daily data at coarser spatial resolution (~4 km; Abatzoglou et al., 2018). European datasets such as E-OBS (Haylock et al., 2008; Cornes et al., 2018) provide daily values but at ∼10 km resolution, which may be insufficient for basin-scale applications in complex terrain (Hofstra et al., 2008, 2010). High-resolution Alpine datasets such as that of Isotta et al. (2014) cover precipitation but not temperature and do not extend to a full 30-year climatological reference period. Uncertainty in gridded products is further sensitive to station density, interpolation method, and grid resolution (Herrera et al., 2019).

To address this gap, we developed a 1-km daily gridded precipitation and temperature dataset for the PRD covering the 1991–2020 climatological reference period. The dataset is based on an extensive multi-source observational network comprising 1,583 precipitation stations and 1,555 temperature stations after quality control and harmonization (details given in Sect. 3.1). Spatial interpolation was performed using Ordinary Kriging for precipitation (Goovaerts, 2000) and Detrended Kriging (DK) for temperature, with elevation as the trend variable, allowing explicit representation of topographic controls on thermal gradients (Bancheri et al., 2018). The resulting dataset provides spatially continuous daily climate fields at 1-km resolution, suitable for hydrological modelling, climate variability assessment, and environmental analysis. To our knowledge, no publicly accessible gridded product simultaneously combines this spatial and temporal resolution over a continuous 30-year period for the Po River District.

2 Study Area

The Po River District is the territory, established by law in 2015, which entirely comprises the Po River, the longest Italian river, with a length of 652 km. The Disctrict territory covers approximately 83,000 km^2 from the southern Alps and northern Apennines to the Adriatic Sea (Fig. 1) - even if the hydrographic basin of the Po River extends to portions of Switzerland and France, for a total area of around 87,000 km^2.

The District comprises an extensive natural hydrographic network consisting of Alpine tributaries, and Apennine rivers, like the ones of Romagna, which drain directly to the Adriatic Sea. This territory is then characterized by numerous landscapes and environments: elevation ranges from sea level to nearly 4,800 m a.s.l., producing strong climatic gradients, affected also by the sea presence in the southern and estearn areas, and pronounced orographic effects (Frei and Schär, 1998). These

https://doi.org/10.5194/essd-2026-467
Preprint. Discussion started: 11 August 2026

characteristics require interpolation methods capable of representing elevation-dependent variability. The topographic data used for interpolation are derived from the European Digital Elevation Model (EU-DEM; Bashfield and Keim, 2011; Copernicus Land Monitoring Service, 2016), validated against independent geodetic measurements across the Alpine domain (Mouratidis et al., 2010; Mouratidis and Ampatzidis, 2019).

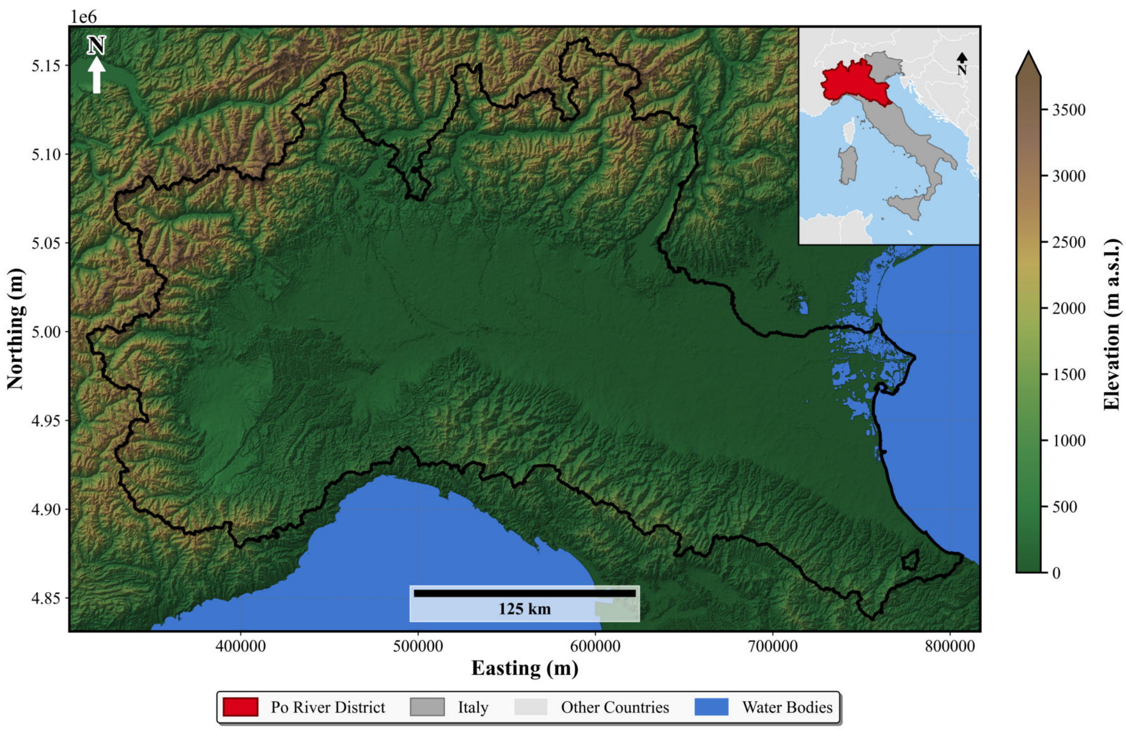

Figure 1. Location of the Po River District (PRD) within Italy and the Digital Elevation Model (EU-DEM) of the study area. Elevation ranges from sea level to approximately 4,800 m a.s.l., illustrating the pronounced topographic gradient from the Alpine headwaters to the Adriatic coastal plain.

3 Multi-source Observational Network and Data Harmonisation

Station data were obtained from regional environmental protection agencies (ARPA) and complemented with observations from the Extended European Alpine Region dataset (EEAR-Clim; Bongiovanni et al., 2025) to reduce boundary effects in geostatistical interpolation. A 20-km buffer surrounding the district's boundary was defined, and all stations located within this buffer were included to stabilise interpolation near domain edges and better constrain orographic gradients across watershed divides.

After harmonization and quality control, the final station network includes 1,583 precipitation stations (1,192 internal ADBPO stations and 391 external EEAR-Clim stations) and 1,555 temperature stations (1,116 internal and 439 external

https://doi.org/10.5194/essd-2026-467
Preprint. Discussion started: 11 August 2026

stations). The spatial distributions of both networks are shown in Fig. 2: panels (a) and (c) illustrate the geographic coverage of precipitation and temperature stations across the PRD and its 20-km buffer zone, respectively, while panels (b) and (d) show the corresponding data availability heatmaps, summarising the fraction of days with valid observations relative to the full 1991–2020 period for each station. The elevation-based distribution of the network and its data availability across the topographic gradient of the PRD are further characterised in Fig. 3: panel (a) shows the number of precipitation and temperature stations across 400-m elevation bins, highlighting the progressive decline in station density above 1,000 m a.s.l., while panel (b) shows the corresponding data availability per elevation band, expressed as the percentage of days with valid observations out of the total 10,957 days of the 1991–2020 period. All station coordinates were reprojected to the Universal Transverse Mercator Zone 32N coordinate reference system (UTM 32N; EPSG:32632), consistent with the spatial grid of the interpolated dataset and the EU-DEM topographic data used for elevation detrending. All time series consist of daily observations defined over the 00:00–24:00 UTC period. Precipitation records represent daily total accumulations (mm day^{-1}), while temperature records represent daily mean values (°C), both standardised following World Meteorological Organization (2018).

3.1 Data Pre-processing and Quality Control

3.1.1 Precipitation Quality Control

Quality control was applied to ensure internal consistency of the merged multi-source dataset. For precipitation, the procedure consisted of record-length screening and automated physical range checks (precipitation $\geq$ 0 mm, in accordance with World Meteorological Organization, 2018), and spatial consistency tests (Klein Tank et al., 2002; Zahradníček et al., 2014). Stations with at least 5% temporal coverage (approximately 18 months) during 1991–2020 were retained to preserve spatial representativeness in high-elevation and sparsely monitored areas. The choice of a minimum temporal coverage threshold of 5% was designed to retain stations in sparsely monitored high-elevation areas while excluding records too short to contribute meaningfully to spatial interpolation. The 20-km buffer width was selected to exceed the typical variogram range in Alpine terrain, ensuring adequate constraint of interpolation near domain boundaries (Goovaerts, 2000). The use of 10 nearest neighbours for spatial consistency checks follows standard practice in geostatistical quality control (Dorninger et al., 2008) and provides a representative local reference while avoiding the inclusion of spatially distant stations with contrasting climatic regimes.

Daily precipitation values were evaluated using a neighbour-based spatial consistency test adapted from buddy-check procedures (Dorninger et al., 2008; Frazier et al., 2016). For each station and date, observations were compared with the 10 nearest stations reporting data on the same day. Stations exhibiting persistent bias greater than 50% relative to neighbours and record lengths shorter than three years were removed from the network. In addition, daily precipitation values equal to or exceeding 40 mm that deviated by more than 50% from the median of the 10 nearest neighbours were flagged and removed. Flagged observations were treated as missing values.

https://doi.org/10.5194/essd-2026-467
Preprint. Discussion started: 11 August 2026

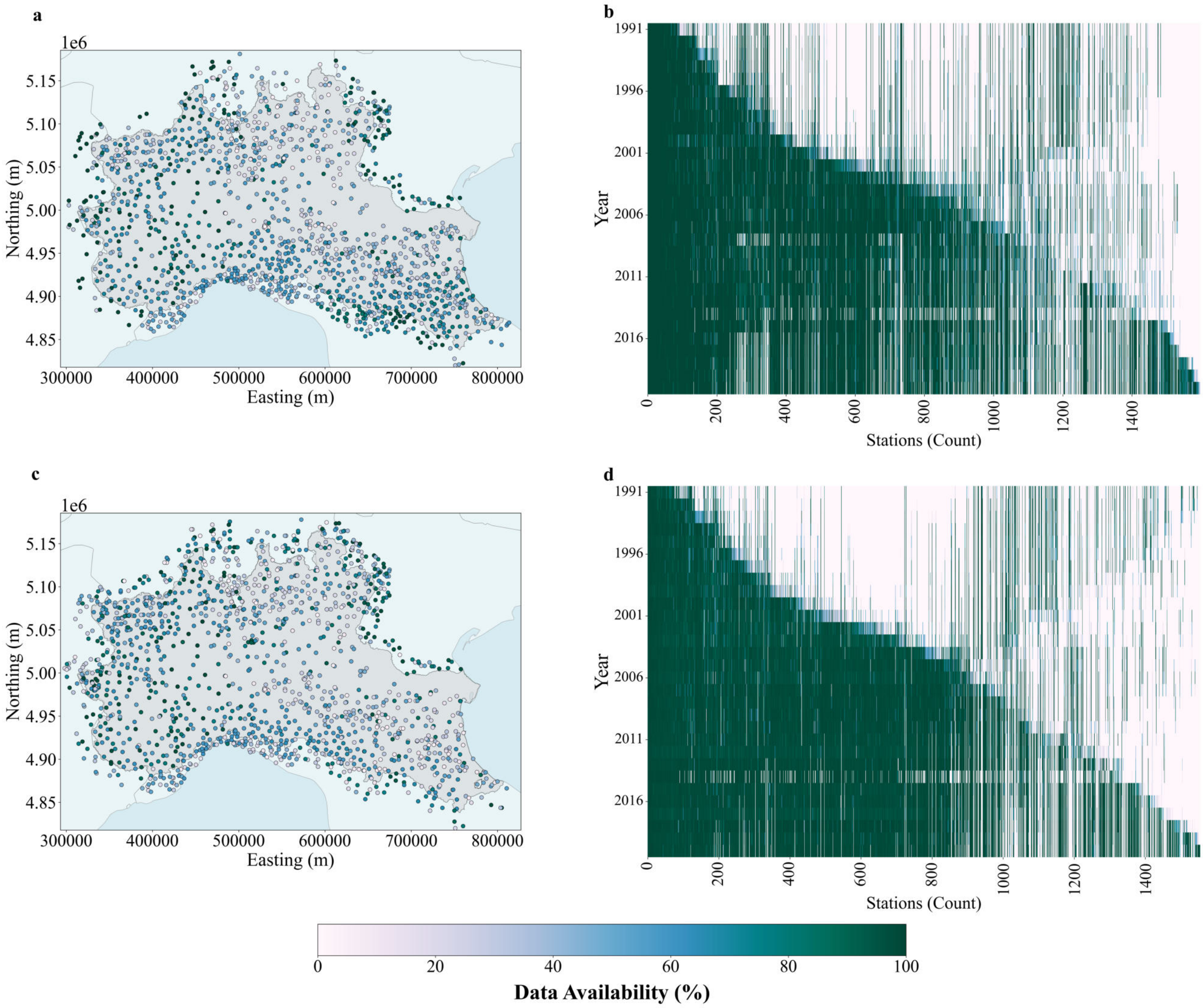

Figure 2. Data availability for precipitation and temperature stations. (a) Spatial distribution of precipitation stations; (b) heatmap of annual data availability (%) for precipitation stations over the 1991–2020 period; (c) spatial distribution of temperature stations; (d) heatmap of annual data availability (%) for temperature stations over the 1991–2020 period. Data availability is expressed as the fraction of days with valid record relative to the full 1991–2020 period, irrespective of each station's operational lifespan.

https://doi.org/10.5194/essd-2026-467
Preprint. Discussion started: 11 August 2026

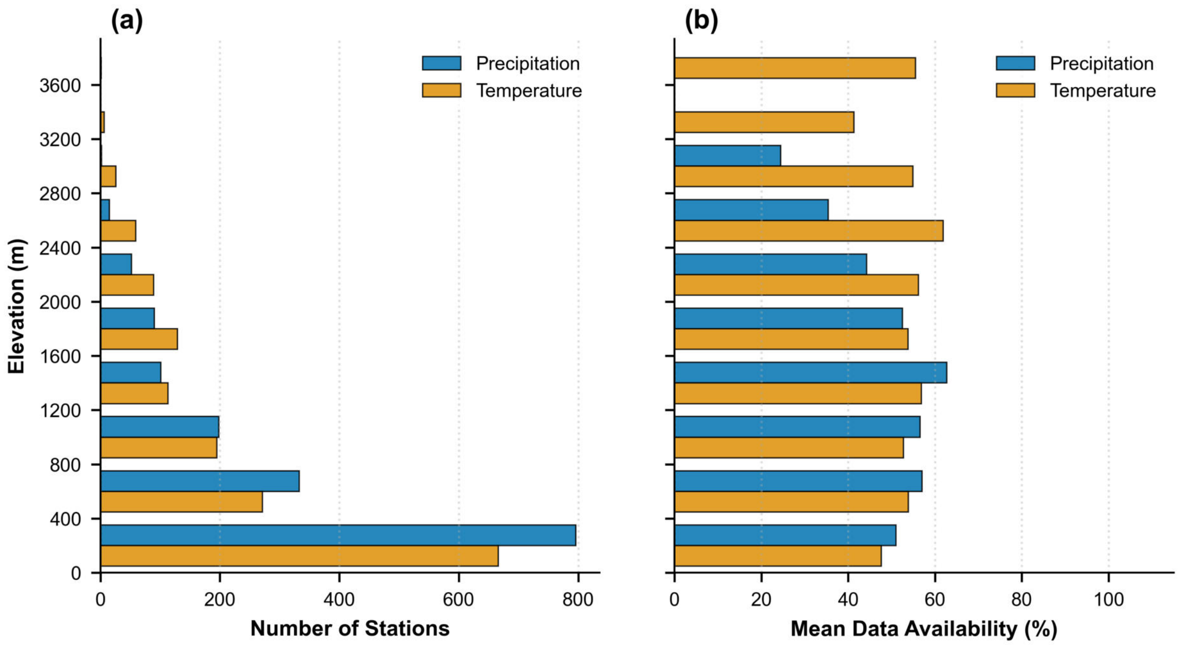

Figure 3. Elevation-based distribution and data availability of the meteorological network. (a) Number of precipitation (blue) and temperature (orange) stations across 400-m elevation bins. (b) Data availability (%) per elevation band for both variables, expressed as the percentage of days with valid observations out of the total 10,957 days of the 1991–2020 period, irrespective of each station's operational lifespan.

3.1.2 Temperature Quality Control

Quality control was applied to ensure internal consistency of the merged multi-source dataset. For temperature, the procedure consisted of record-length screening and automated physical range checks (temperature within -40 to $+50$ °C, in accordance with World Meteorological Organization, 2018), and temporal consistency tests (Klein Tank et al., 2002; Zahradníček et al., 2014). Stations with at least 5% temporal coverage (approximately 18 months) during 1991–2020 were retained to preserve spatial representativeness in high-elevation and sparsely monitored areas.

Given the strong elevation dependency of temperature, a temporal consistency approach was adopted for quality control, following Dorninger et al. (2008) and Gebrechorkos et al. (2023). For each station i and date t, the daily temperature change was computed as:

$$\Delta T_i(t) = T_i(t) - T_i(t-1) \tag{1}$$

and compared against the median daily change of the 10 nearest stations with available observations on the same date:

$$\Delta T_{\text{median}}(t) = \text{median}\{\Delta T_j(t) : j \in \mathcal{N}_i, j \neq i\} \tag{2}$$

https://doi.org/10.5194/essd-2026-467
Preprint. Discussion started: 11 August 2026

where $\mathcal{N}_i$ denotes the set of the 10 nearest active neighbours of station i on date t. An observation was flagged as potentially erroneous if:

$$\left|\Delta T_i(t) - \Delta T_{\mathrm{median}}(t)\right| > \max\left(0.30 \times \left|\Delta T_{\mathrm{median}}(t)\right|,\, 3\,^{\circ}\mathrm{C}\right) \tag{3}$$

This mixed criterion combines a relative threshold (30%) with an absolute floor of 3 °C. The absolute floor prevents pathological behaviour on days when $\Delta T_{\mathrm{median}}$ approaches zero — a condition that would otherwise render a purely relative threshold hypersensitive to noise — while the relative component ensures proportionate flagging during rapid synoptic transitions such as frontal passages, when basin-wide temperature changes of 10–15 °C within a single day are physically plausible over Alpine terrain (Zahradníček et al., 2014). Flagged observations were subject to manual inspection; confirmed erroneous values were removed and treated as missing data. The neighbourhood $\mathcal{N}_i$ is recomputed at each time step to include only stations reporting data on that date, ensuring that the reference median remains representative of the contemporaneous synoptic signal rather than a climatological average.

3.2 Spatial Interpolation Framework

Daily observations from the final stations network were interpolated to a continuous 1-km resolution grid using the GEOframe kriging framework (Bancheri et al., 2018). Both approaches are built upon the Ordinary Kriging (OK) framework (Goovaerts, 2000; Hengl et al., 2007), with semivariogram models selected adaptively at each daily time step as described below. For precipitation, spatial interpolation was performed using OK. At any unsampled grid point x_0, the estimated precipitation $\hat{Z}(x_0)$ is expressed as:

$$\hat{Z}(x_0) = \sum_{i=1}^{n} \lambda_i Z(x_i) \tag{4}$$

where $Z(x_i)$ are the observed values at the n neighbouring stations and λ_i are the kriging weights. These weights are obtained by solving the OK system:

$$\begin{pmatrix} \Gamma & \mathbf{1} \\ \mathbf{1}^T & 0 \end{pmatrix} \begin{pmatrix} \lambda \\ \mu \end{pmatrix} = \begin{pmatrix} \gamma_0 \\ 1 \end{pmatrix} \tag{5}$$

where Γ is the $(n \times n)$ matrix of semivariance values between observation pairs, γ_0 is the vector of semivariances between each observation station and the target point x_0, and μ is the Lagrange multiplier enforcing $\sum_{i=1}^{n} \lambda_i = 1$.

3.2.1 Variogram Model Selection

At each daily time step, the empirical semivariogram was first computed as:

$$\hat{\gamma}(h) = \frac{1}{2N(h)} \sum_{i=1}^{N(h)} [Z(x_i) - Z(x_i + h)]^2 \tag{6}$$

where h is the Euclidean separation distance between station pairs and $N(h)$ is the number of pairs within the distance lag h. The empirical semivariogram was then fitted to a candidate set of five theoretical models implemented in GEOframe-SIK

https://doi.org/10.5194/essd-2026-467
Preprint. Discussion started: 11 August 2026

Open Access Earth System Science Data Discussions

(Bancheri et al., 2018): Exponential, Gaussian, Linear, Power, and Spherical. Model parameters — nugget c_0, partial sill c, range a, and shape exponent ω for the Power model — were optimised using Particle Swarm Optimisation (PSO), minimising the residuals between the empirical and each theoretical semivariogram. The model yielding the best fit at each time step was then selected for kriging interpolation. Following the notation of Bancheri et al. (2018), the five models are defined as:

$$\gamma_{\mathrm{Exp}}(h) = c_0 + c\left(1 - e^{-h/a}\right) \tag{7}$$

$$\gamma_{\mathrm{Gau}}(h) = c_0 + c\left[1 - e^{-(h/a)^2}\right] \tag{8}$$

$$\gamma_{\mathrm{Lin}}(h) = \begin{cases} c_0 + c\,\dfrac{h}{a} & h < a \\ c_0 + c & h \geq a \end{cases} \tag{9}$$

$$\gamma_{\mathrm{Pow}}(h) = c_0 + c\,h^{\omega} \tag{10}$$

$$\gamma_{\mathrm{Sph}}(h) = \begin{cases} c_0 + c\left[1.5\,\dfrac{h}{a} - 0.5\left(\dfrac{h}{a}\right)^3\right] & h < a \\ c_0 + c & h \geq a \end{cases} \tag{11}$$

where c_0 is the nugget, c is the partial sill, a is the range parameter, and $\omega \in (0,2)$ is the shape exponent of the Power model, all optimised via PSO at each daily time step.

3.2.2 Detrended Kriging for Temperature

For temperature, spatial interpolation was performed using Detrended Kriging (DK) as implemented in the GEOframe-SIK package (Bancheri et al., 2018). Temperature exhibits a well-documented dependency on elevation in Alpine terrain (Rolland, 2003); DK explicitly accounts for this by removing the elevation-dependent trend prior to kriging interpolation.

At each daily time step t, a linear regression between observed temperatures and station elevations was computed across all active stations in the network:

$$T(z,t) = \beta_0(t) + \beta_1(t) \cdot z \tag{12}$$

where $\beta_0(t)$ is the intercept and $\beta_1(t)$ is the empirically estimated lapse rate for day t, allowing the thermal gradient to vary in response to prevailing atmospheric conditions. Observed temperatures were then detrended by removing the elevation-dependent component:

$$T_{\mathrm{detrended}}(x_i,t) = T_{\mathrm{observed}}(x_i,t) - \beta_1(t) \cdot z_i \tag{13}$$

Ordinary Kriging was applied to the detrended residuals, and the final temperature estimate at target grid point x_0 with elevation z_0 was reconstructed as:

$$\hat{T}(x_0,t) = \hat{T}_{\mathrm{detrended}}(x_0,t) + \beta_1(t) \cdot z_0 \tag{14}$$

https://doi.org/10.5194/essd-2026-467
Preprint. Discussion started: 11 August 2026

This approach allows the lapse rate to adapt to day-to-day variability in atmospheric conditions, rather than relying on a fixed environmental lapse rate, and is consistent with the DK formulation described in Bancheri et al. (2018).

4 Cross-Validation and Uncertainty Assessment

To assess the accuracy of the kriging interpolation, we employed leave-one-out cross-validation (LOO-CV) (Harris et al., 2020; Hengl et al., 2007). This method provides unbiased error estimates by iteratively withholding each station i (where $i = 1, \ldots, N$) from the interpolation and predicting its value $\hat{Z}(x_i)$ using the remaining $N-1$ stations. The prediction error $e_i = \hat{Z}(x_i) - Z(x_i)$ and the kriging variance $\sigma_k^2(x_i)$ were recorded for all stations across the entire study period (1991–2020), generating approximately $N \times T$ validation points.

4.1 Performance Metrics

The modified Kling–Gupta Efficiency (Gupta et al., 2009) was adopted as the primary performance benchmark for both precipitation and temperature. The KGE integrates three complementary diagnostic components — temporal correlation (r), variability ratio (α), and a bias term (β) — into a single dimensionless score bounded above by unity:

$$KGE = 1 - \sqrt{(r-1)^2 + (\alpha-1)^2 + (\beta-1)^2} \tag{15}$$

where $\alpha = \sigma_{\hat{Z}}/\sigma_Z$ quantifies the ratio of estimated to observed variability. The bias term (β) follows the modified KGE definition for both variables:

$$\beta = \frac{\mu_{\hat{Z}} - \mu_Z}{\sigma_Z} \tag{16}$$

By using the same bias formulation for both precipitation and temperature, we maintain a dimensionless and internally consistent performance metric across variables. This unified approach ensures methodological consistency while allowing for a direct comparison of interpolation performance between the two climate variables throughout the study domain.

4.2 Complementary Statistics

In addition to KGE, four complementary statistics were computed for both variables to ensure comparability with existing datasets and to provide a complete characterisation of interpolation errors. The Pearson correlation coefficient (CC) measures the linear correspondence between observed and estimated values. The Mean Absolute Error (MAE) provides a robust, outlier-insensitive measure of average error magnitude. The Root Mean Square Error (RMSE) amplifies the contribution of large deviations and is therefore sensitive to extreme errors. Bias is expressed as a dimensionless ratio for precipitation, where the strictly positive nature of the variable renders relative deviations physically meaningful, and as an absolute difference (°C) for temperature, where ratio-based metrics become ill-defined as mean daily temperatures approach 0°C.

https://doi.org/10.5194/essd-2026-467
Preprint. Discussion started: 11 August 2026

Table 1. Continuous statistical indices used for cross-validation of interpolated fields.

Statistic	Equation	Optimal Value
MAE	$\frac{1}{N}\sum_{i=1}^{N}\lvert Z(x_i)-\hat{Z}(x_i)\rvert$	0
CC	$\frac{\sum(\hat{Z}(x_i)-\bar{\hat{Z}})(Z(x_i)-\bar{Z})}{\sqrt{\sum(\hat{Z}(x_i)-\bar{\hat{Z}})^2\sum(Z(x_i)-\bar{Z})^2}}$	1
RMSE	$\sqrt{\frac{1}{N}\sum(\hat{Z}(x_i)-Z(x_i))^2}$	0
Bias (Precip)	$100\times\left(\frac{\bar{\hat{Z}}}{\bar{Z}}-1\right)$	0
Bias (Temp)	$\bar{\hat{Z}}-\bar{Z}$	0
KGE	$1-\sqrt{(r-1)^2+(\alpha-1)^2+(\beta-1)^2}$	1

4.3 Wet-Days versus All-Days Analysis

A persistent artefact in gridded precipitation datasets produced by spatial interpolation is the so-called drizzle effect: the smoothing inherent to Kriging tends to redistribute low precipitation amounts across broad areas on days when rainfall is spatially localised, inflating wet-day frequency while suppressing peak intensities (Goovaerts, 2000; Bourgault, 2021). To transparently characterise this behaviour, all performance metrics were computed under two complementary scenarios:

- **All-Days Analysis:** encompassing all 10,957 days in the 1991–2020 study period, providing an assessment of overall climatological performance and total water balance.
- **Wet-Days Analysis:** restricted to days on which the withheld station recorded precipitation ≥ 0.1 mm, enabling evaluation of the model's ability to reproduce the intensity and temporal structure of actual rainfall events independently of the interpolation of dry periods.

The wet-day threshold of 0.1 mm is consistent with the minimum detection limit of tipping-bucket gauges widely deployed across the ARPA network (World Meteorological Organization, 2018) and follows the convention adopted in high-resolution Alpine precipitation analyses (Frei and Schär, 1998; Isotta et al., 2014). Although a higher threshold of 1 mm is used in some European gridded products (Haylock et al., 2008; Cornes et al., 2018), the 0.1 mm criterion was retained here to preserve the full dynamic range of observed precipitation and to avoid artificially inflating dry-day frequency in the interpolated fields. All statistical indices and defining equations are summarised in Table 1.

https://doi.org/10.5194/essd-2026-467
Preprint. Discussion started: 11 August 2026

5 Technical Validation

The leave-one-out cross-validation results (see Fig. 4) demonstrate that the kriging framework reproduces daily climate variability with strong agreement against station observations over the 1991–2020 study period. Across the full stations network, precipitation achieves mean KGE values exceeding 0.84, while temperature exceeds 0.88, indicating high overall interpolation skill across the complex Alpine–Po Basin domain.

Under All-Days conditions, precipitation exhibits a mean KGE of 0.84 and a Pearson correlation coefficient of 0.90, with a mean absolute error (MAE) of 1.28 mm, a root mean square error (RMSE) of 3.79 mm, and a mean bias of $+1.07\%$. Restricting the evaluation to Wet-Days ($\geq$ 0.1 mm) results in a moderate reduction in skill (KGE = 0.82; CC = 0.88), accompanied by higher MAE (3.05 mm) and RMSE (6.02 mm) and a shift toward underestimation (bias = -4.33%). This attenuation of high precipitation intensities under Wet-Days conditions is consistent with the conditional bias characteristics of kriging estimators and smoothing effects documented in geostatistical rainfall interpolation (Goovaerts, 2000; Bourgault, 2021).

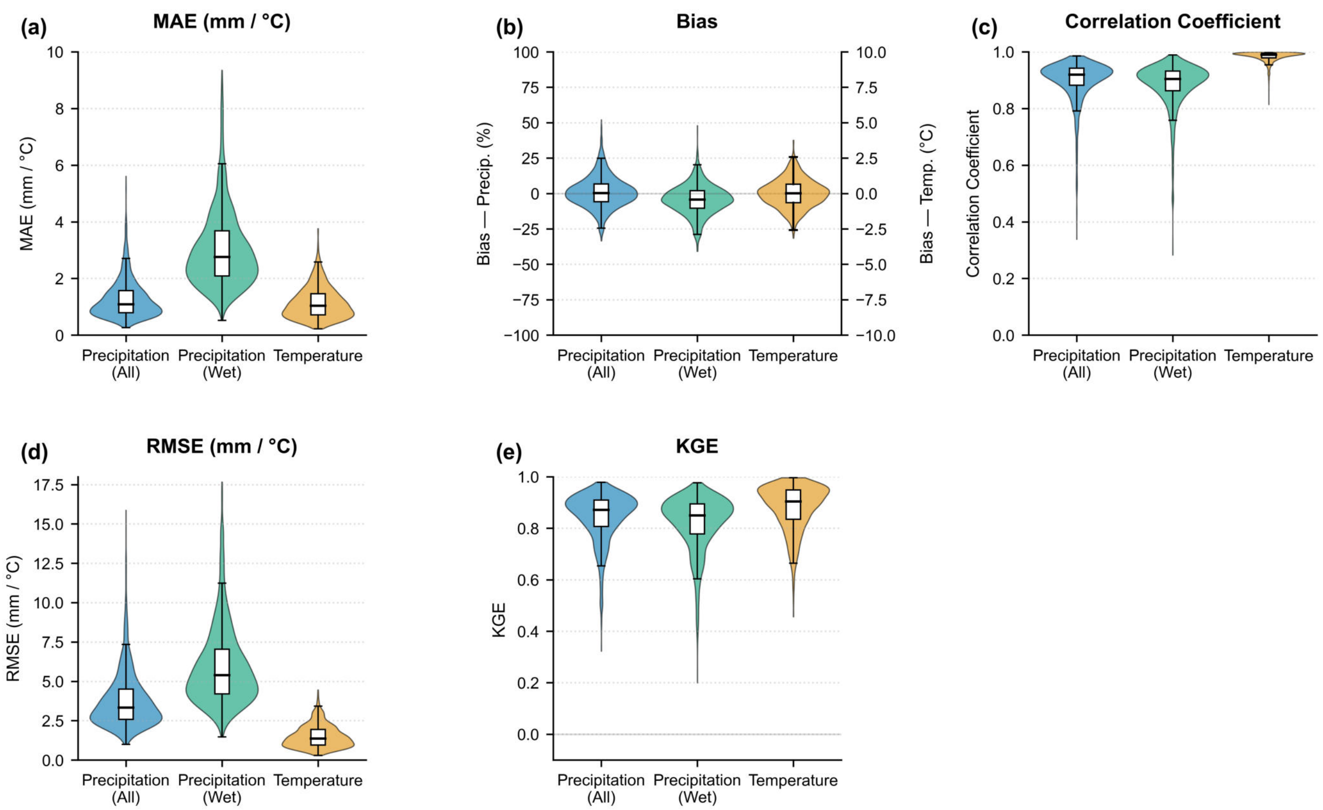

Figure 4. Distribution of cross-validation performance metrics across all stations for precipitation (All-Days and Wet-Days) and temperature. Inner boxes show the interquartile range and median; violin bodies represent the full distribution. For the Bias panel, precipitation (%) is referenced on the left y-axis and temperature ($^\circ$C) on the right y-axis, reflecting the differing physical scales of the two variables.

https://doi.org/10.5194/essd-2026-467
Preprint. Discussion started: 11 August 2026

Open Access Earth System Science Data Discussions

Temperature interpolation exhibits greater stability, consistent with the smoother spatial structure of temperature fields relative to precipitation. Cross-validation yields a mean KGE of 0.88, correlation of 0.98, MAE of 1.14 °C, RMSE of 1.5 °C, and negligible bias (+0.02 °C). The elevation-detrending procedure applied prior to kriging follows established physiographically informed interpolation approaches (Daly et al., 2008; Goovaerts, 2000), effectively removing the large-scale altitudinal gradient and limiting systematic elevation-related bias across the approximately 4,800 m relief range of the basin.

Spatial diagnostics (see Fig. 5) reveal geographically structured error patterns for precipitation. Elevated MAE and reduced KGE are concentrated in high-elevation northern sectors and along southern boundary regions, where orographic gradients are strongest. Similar spatial heterogeneity in precipitation fields has been reported in Alpine climatological analyses (Frei and Schär, 1998; Isotta et al., 2014). In contrast, central lowland areas exhibit lower errors and more homogeneous performance, and these spatial gradients are less pronounced for temperature.

Elevation-stratified regression analysis (see Fig. 6) confirms a statistically significant decline in performance with increasing altitude. Reduced interpolation skill in high-relief terrain reflects enhanced spatial variability and sampling challenges in mountainous regions, consistent with previous geostatistical investigations incorporating elevation effects (Goovaerts, 2000; Daly et al., 2008; Ossa-Moreno et al., 2019). For precipitation, MAE increases by approximately 0.54 mm per 1000 m (All-Days) and 0.87 mm per 1000 m (Wet-Days), while RMSE increases by approximately 1.08 mm and 1.33 mm per 1000 m, respectively (all $p < 0.001$). Temperature MAE and RMSE increase by approximately 0.28 °C and 0.38 °C per 1000 m ($p < 0.001$). Bias becomes increasingly negative with elevation for both variables, and both CC and KGE decrease significantly with height.

The annual heatmaps of cross-validation performance (see Fig. 7) reveal a gradual improvement in interpolation skill over the study period. Progressive improvements in European climate datasets have been linked to enhanced station coverage, homogenisation procedures, and quality control (Klein Tank et al., 2002; Herrera et al., 2019). For precipitation under All-Days conditions, KGE increases from approximately 0.76–0.78 in the early 1990s to 0.83–0.84 in the mid-2010s, accompanied by modest reductions in MAE and RMSE. Temperature metrics remain comparatively stable throughout the period. No abrupt structural shifts or systematic long-term degradation are evident in any metric, indicating temporal robustness of the interpolation framework over the full 30-year climatological period.

https://doi.org/10.5194/essd-2026-467
Preprint. Discussion started: 11 August 2026

Open Access Earth System Science Data Discussions

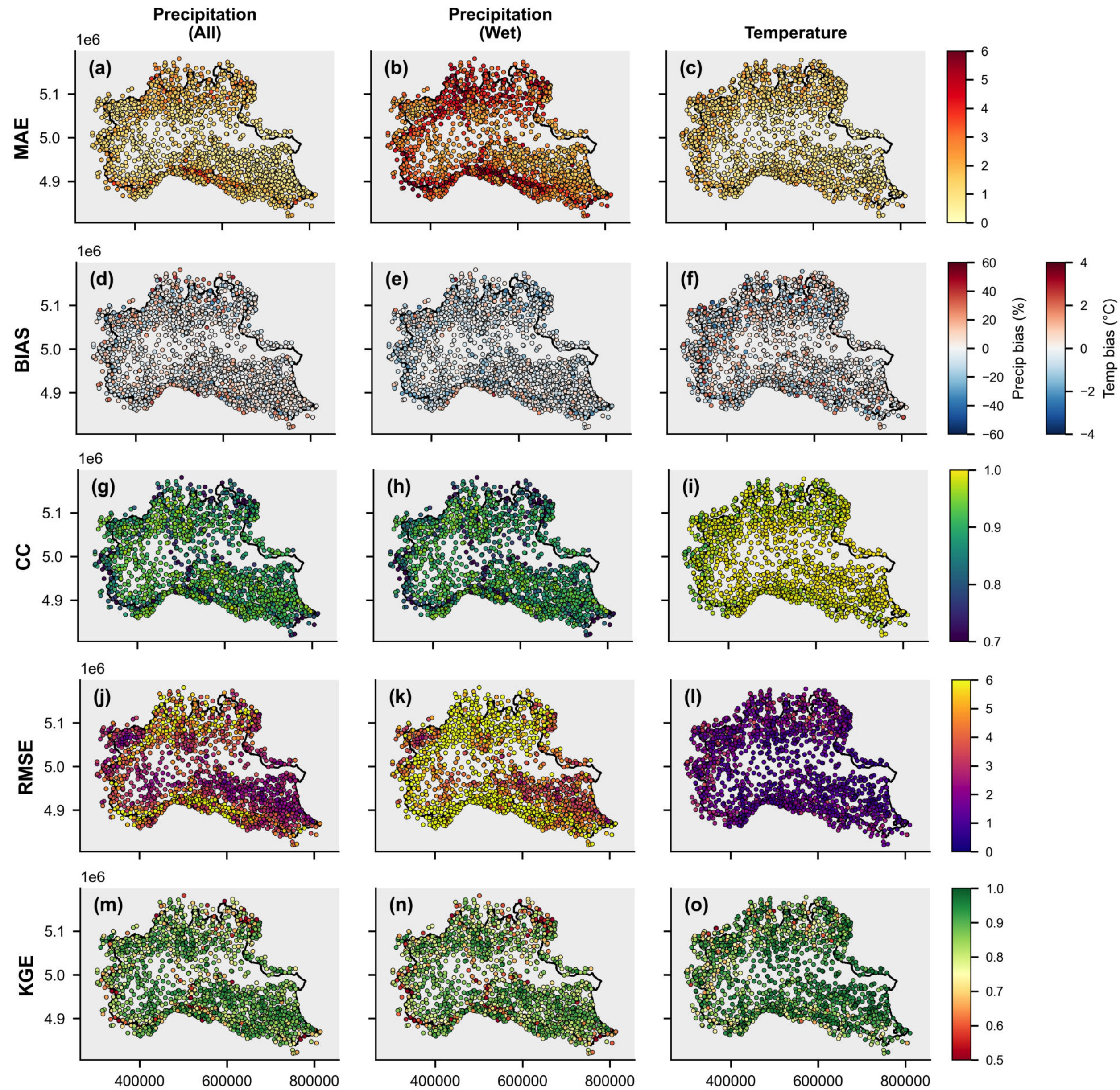

Figure 5. Spatial distribution of leave-one-out cross-validation performance metrics across the station network for precipitation (All-Days and Wet-Days) and temperature. Rows show MAE, Bias, Pearson correlation coefficient (CC), RMSE, and KGE from top to bottom. For Bias, separate colour scales are used for precipitation (%) and temperature (°C).

https://doi.org/10.5194/essd-2026-467
Preprint. Discussion started: 11 August 2026

Open Access Earth System Science Data Discussions

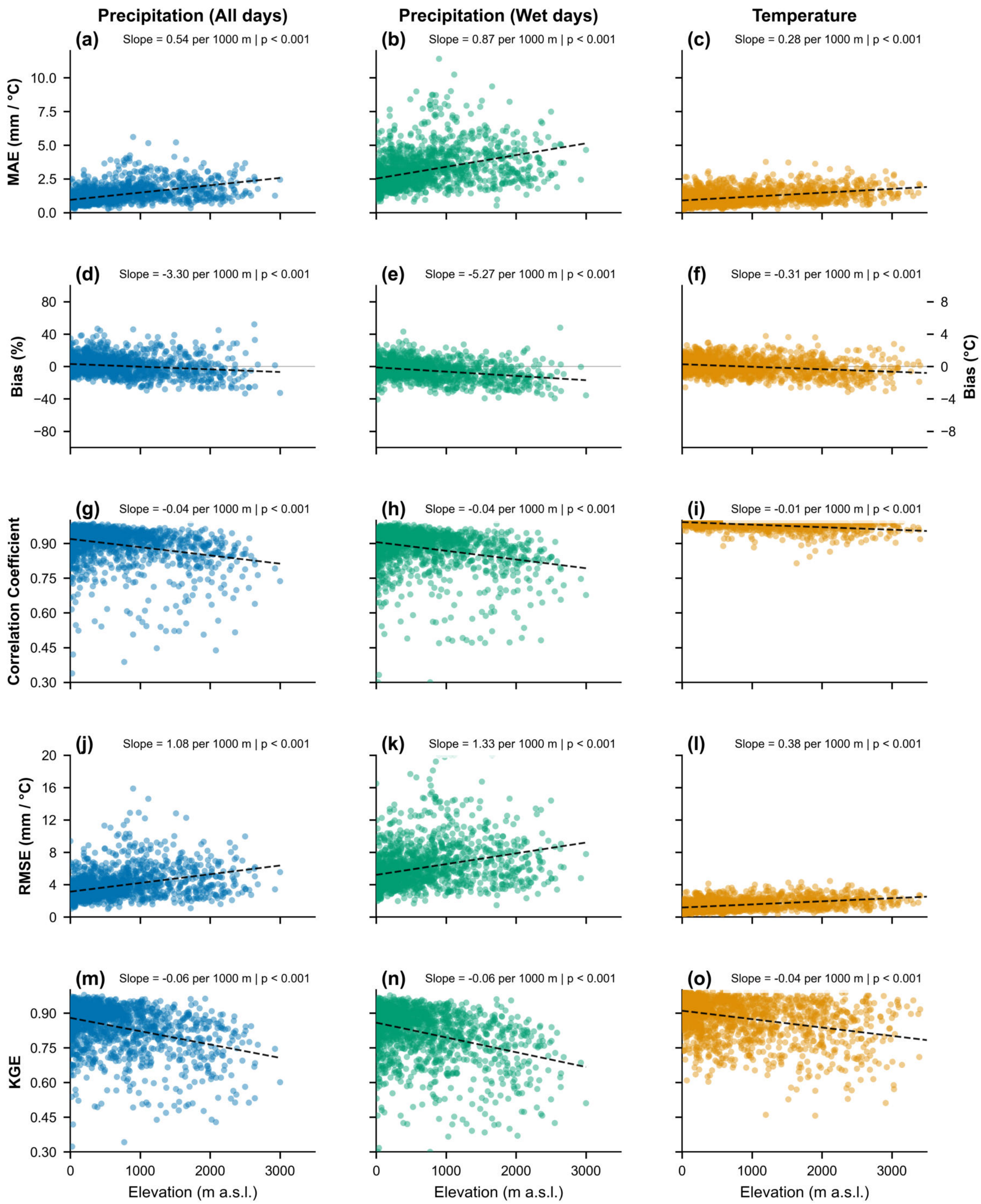

Figure 6. Relationship between station elevation and cross-validation performance metrics for precipitation interpolation (All-Days and Wet-Days) and temperature. Each point represents one station; dashed lines indicate ordinary least-squares regression trends. Note that the Bias y-axis scale differs between precipitation (%) and temperature ($^{\circ}$C), shown on the left and right axes of the respective panels.

https://doi.org/10.5194/essd-2026-467
Preprint. Discussion started: 11 August 2026

5.1 Dataset Consistency

Given the progressive evolution of the station network during the 1991–2020 period and the inclusion of external buffer stations to mitigate boundary effects, a dataset consistency assessment was performed to ensure that no artificial discontinuities were introduced into the gridded climate fields. This evaluation focused on detecting structural shifts in interpolation performance over time and quantifying the sensitivity of the dataset to network configuration.

Annual heatmaps of cross-validation performance metrics (see Fig. 7) provide the primary diagnostic of temporal consistency. For precipitation under All-Days conditions, mean KGE increases from approximately 0.76–0.78 in the early 1990s to values exceeding 0.83–0.84 in the mid-2010s, accompanied by a gradual reduction in MAE and RMSE. A similar, though less pronounced, trend is observed under Wet-Days conditions. Temperature metrics remain comparatively stable throughout the period, with KGE consistently above 0.85 and only minor interannual fluctuations in MAE and RMSE. Importantly, no abrupt step changes or discontinuities are evident in any metric, suggesting that modifications in station density or pre-processing procedures did not introduce structural breaks in the dataset (Zahradníček et al., 2014).

Spatially aggregated climatologies computed separately for early (1991–2000), middle (2001–2010), and late (2011–2020) decades exhibit consistent large-scale patterns, with no artificial spatial discontinuities detected between decades. Elevation-dependent trends in error metrics (see Fig. 6) also remain stable when evaluated separately for each decade, confirming that the altitude-related degradation in interpolation skill reflects persistent topographic controls rather than temporal inconsistencies.

Overall, the combination of annual performance diagnostics, network sensitivity experiments, and decade-wise spatial comparisons indicates that the 1-km daily precipitation and temperature dataset is temporally coherent and structurally robust over the full 30-year climatological period. Improvements in validation metrics occur gradually and continuously, consistent with progressive network densification (Herrera et al., 2019), and are not associated with abrupt methodological artefacts.

6 Comparative Characterisation Against Regional Gridded Datasets

To contextualise the spatial performance of the 1-km Kriging dataset, it was benchmarked against two widely used regional gridded climate products: E-OBS (v31.0e; Cornes et al., 2018) and EMO-1arcmin (Salamon et al., 2026). Both products serve as standard references in European observational climatology and provide a meaningful baseline against which resolution-dependent differences in spatial fidelity, temperature extremes, and precipitation characteristics can be systematically evaluated.

The 1-km Kriging dataset resolves fine-scale spatial heterogeneity across the PRD that remains undetectable in coarser gridded products (Fig. 8). To evaluate resolution-dependent performance under climatically extreme conditions, two benchmark periods were selected. The summer of 2003 — the most thermally extreme season within the 1991–2020 reference period — provides a stringent test case for the representation of compound heat-drought extremes. Storm Alex (October 2020), the most intense precipitation event of the study period, serves as a critical benchmark for assessing each product's capacity to resolve extreme rainfall magnitudes.

https://doi.org/10.5194/essd-2026-467
Preprint. Discussion started: 11 August 2026

Open Access Earth System Science Data Discussions

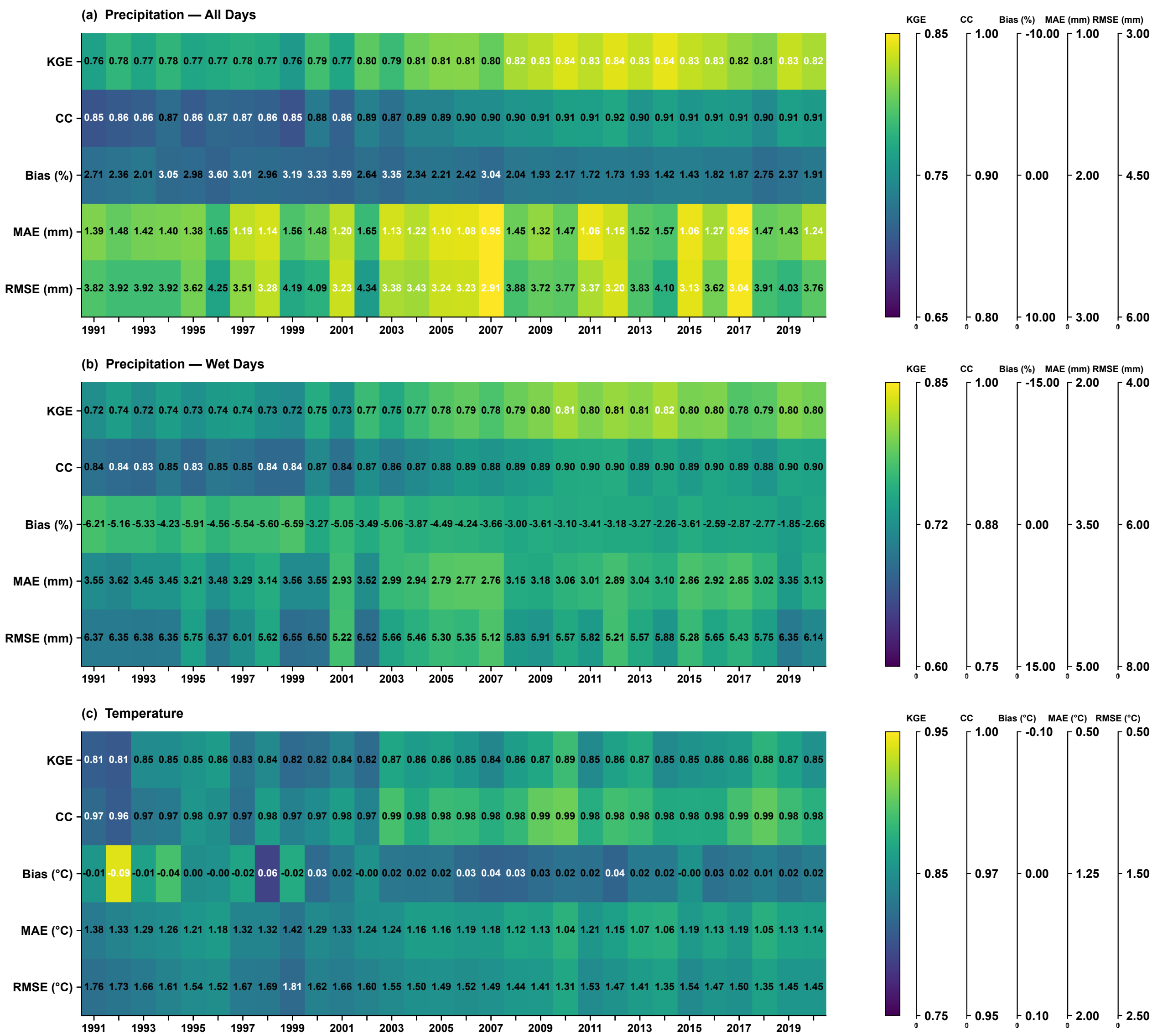

Figure 7. Annual mean cross-validation performance metrics over the 1991–2020 period for (a) precipitation interpolation evaluated on all days, (b) precipitation interpolation evaluated on wet days only (observed precipitation ≥ 0.1 mm), and (c) temperature interpolation. Each row of a heatmap corresponds to one performance metric — KGE, Pearson correlation coefficient (CC), Bias, MAE, and RMSE — and each column represents a calendar year. Cell values show the mean metric computed across all stations with valid data in that year. The colour scale (viridis) is normalised such that dark colours indicate poor performance and bright colours indicate good performance, regardless of whether the metric is higher-better (KGE, CC) or lower-better (Bias, MAE, RMSE). Individual scale bars on the right of each panel show the corresponding raw value range for each metric. Bias is expressed as a percentage for precipitation and as an absolute difference in °C for temperature.

https://doi.org/10.5194/essd-2026-467
Preprint. Discussion started: 11 August 2026

Under mean climatological conditions, the high-resolution product captures sharp topographic gradients and localised climate features that are systematically smoothed in the 10-km E-OBS grid. This distinction is particularly evident in temperature extremes: the 1-km dataset resolves minimum annual temperatures reaching $-11.1°C$, compared to $-4.7°C$ in E-OBS and $-9.8°C$ in EMO, indicating that pixel-averaging in coarser grids progressively suppresses the thermal signature of high-altitude areas. During Storm Alex (2–3 October 2020), which most severely affected the Roya valley and Maritime Alps along the French–Italian border but produced extreme precipitation across western Piedmont within the PRD, these differences are further amplified: the maximum three-day accumulated precipitation reaches 482 mm in the 1-km product within the western Piedmont sector, whereas E-OBS captures only 277 mm — a reduction of approximately 43% — indicating a substantial loss of extreme signal intensity at coarser resolutions. Together, these results indicate that kilometre-scale topographic forcing, a key driver of local climate variability in complex terrain, can only be meaningfully represented when spatial resolution is commensurate with the scale of the underlying physiographic gradients (Aalto et al., 2014; Steinacker et al., 2006).

Further evidence of resolution-dependent performance emerges from the analysis of annual temperature anomalies over the 1991–2020 period (Fig. 9). The ridge plots reveal that all three products capture the basin-scale warming trend; however, the 1-km dataset consistently resolves a broader and more symmetric anomaly distribution, reflecting greater sensitivity to local thermal contrasts across the heterogeneous landscape of the PRD. In contrast, EMO exhibits a progressive warm bias, most pronounced after 2013, suggesting a systematic departure in its representation of near-surface temperatures in recent years. E-OBS displays notably compressed distribution tails, indicating that grid-cell averaging at 10-km resolution inherently underrepresents the spatial variability of temperature extremes — a limitation with direct implications for heatwave and frost risk assessments that depend on the accurate characterisation of local thermal regimes (Beck et al., 2018).

The representation of seasonal precipitation characteristics reveals systematic differences across datasets with direct implications for hydrological applications (Fig. 10). The 1-km Kriging product resolves a broader distribution of wet-day counts across all seasons, reflecting its capacity to represent sub-grid precipitation variability that is inherently averaged out in coarser products. This is a direct consequence of spatial resolution: as grid spacing increases, precipitation is distributed over larger areas, reducing the number of grid cells that exceed the wet-day threshold while simultaneously inflating mean intensities on precipitation days — a well-documented artefact of spatial averaging that distorts the frequency–intensity relationship of rainfall (Hofstra et al., 2010; Ntagkounakis et al., 2025). The 1-km dataset resolves this relationship more continuously across the intensity spectrum, particularly during the flood-prone autumn season (SON), suggesting an improved representation of the convective and orographic processes that govern precipitation variability in this region. These characteristics indicate that the 1-km Kriging dataset may provide a more physically consistent and operationally relevant basis for local-scale hydrological modelling and extreme event analysis, where the accurate partitioning of precipitation frequency and intensity is essential.

https://doi.org/10.5194/essd-2026-467
Preprint. Discussion started: 11 August 2026

Open Access Earth System Science Data Discussions

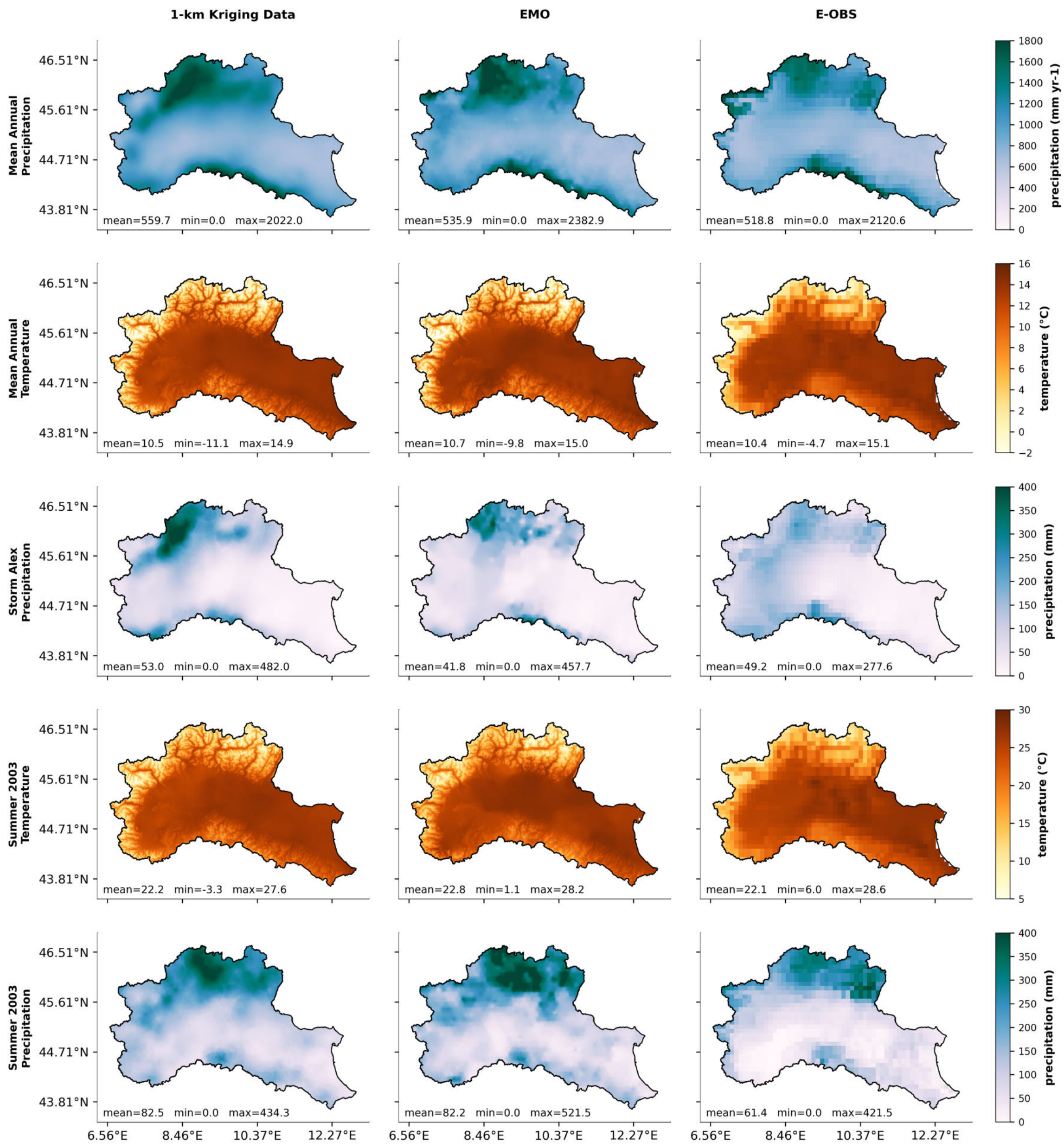

Figure 8. Spatial distribution of temperature and precipitation variables across the three gridded datasets. Rows show (from top to bottom): mean annual precipitation, mean annual temperature, total precipitation during Storm Alex (October 2020), summer 2003 mean temperature, and summer 2003 total precipitation. Columns correspond to the 1-km Kriging dataset (left), EMO (centre), and E-OBS (right). Values below each panel report the spatial mean, minimum, and maximum over the PRD.

https://doi.org/10.5194/essd-2026-467
Preprint. Discussion started: 11 August 2026

Open Access Earth System Science Data Discussions

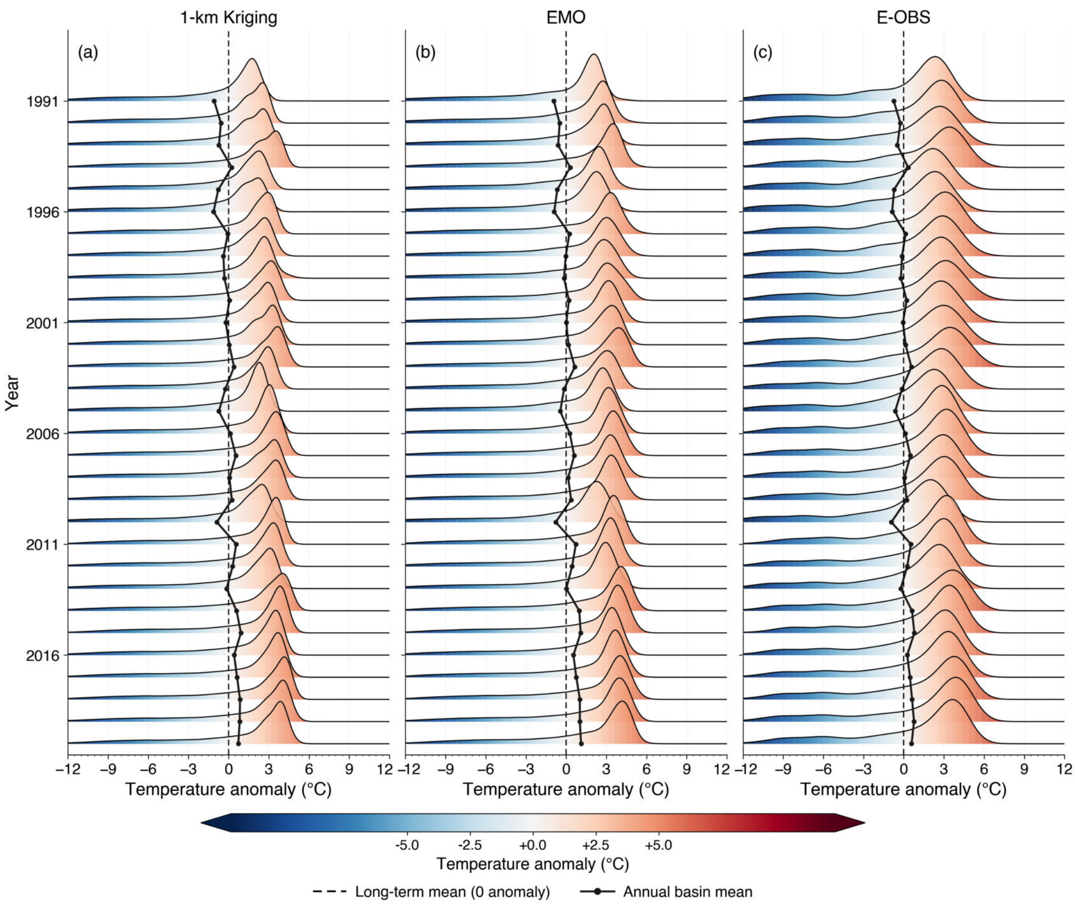

Figure 9. Annual temperature anomaly distributions for the 1991–2020 period. Each ridge represents the frequency distribution of daily grid-cell temperature anomalies aggregated annually across the PRD. Panels (a), (b), and (c) correspond to the 1-km Kriging dataset, EMO, and E-OBS, respectively. The black line connects annual basin-mean anomalies; the dashed vertical line indicates the long-term mean (zero anomaly). Colours indicate the sign and magnitude of the anomaly, ranging from blue (negative) to red (positive).

https://doi.org/10.5194/essd-2026-467
Preprint. Discussion started: 11 August 2026

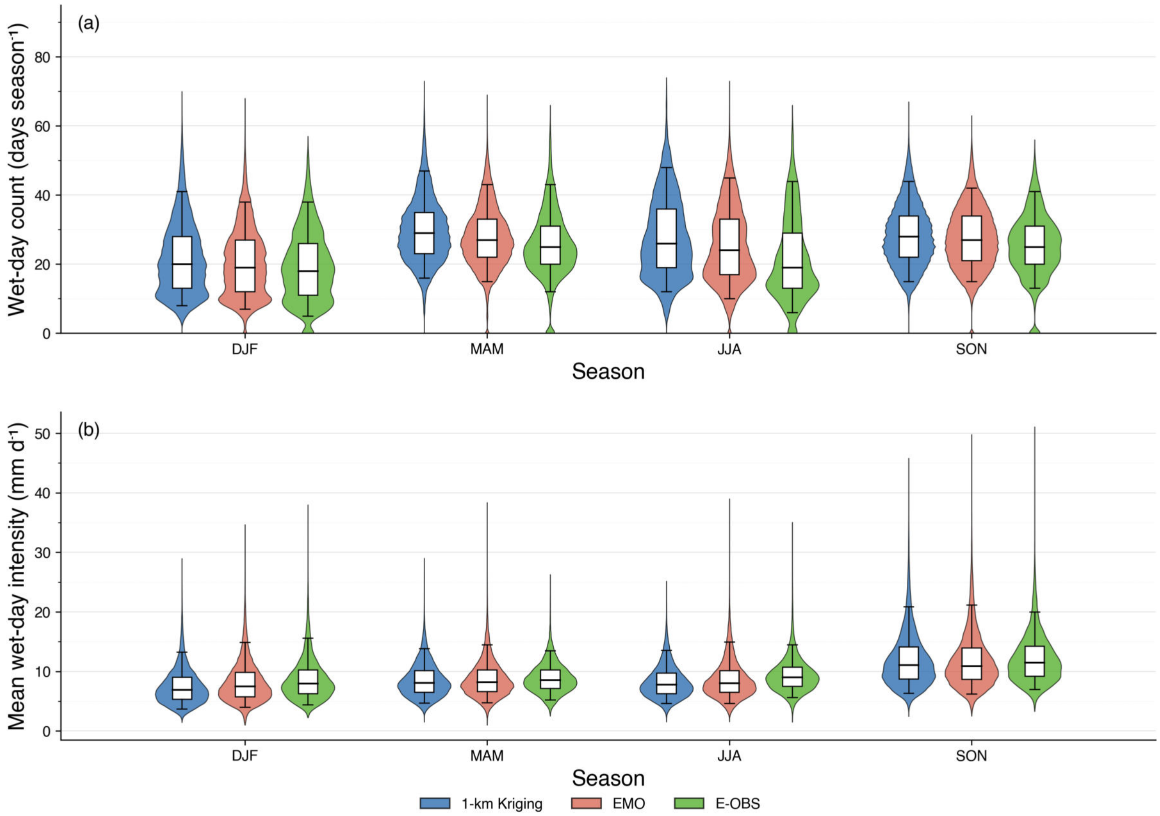

Figure 10. Seasonal precipitation characteristics per grid cell over the 1991–2020 period. Violin plots show the distribution of (a) wet-day frequency (days season^{-1}, threshold: $\geq$1 mm day^{-1}) and (b) mean wet-day intensity (mm day^{-1}) across all grid cells for each season: December–February (DJF), March–May (MAM), June–August (JJA), and September–November (SON). Blue, orange, and green violins correspond to the 1-km Kriging dataset, EMO, and E-OBS, respectively. Embedded box plots show the interquartile range and median.

7 Usage Notes

The dataset is distributed as annual NetCDF files containing daily gridded precipitation and temperature fields at 1-km spatial resolution. Each year is provided as two separate files (e.g., `precipitation_1991.nc` and `temperature_1991.nc`), following Climate and Forecast (CF) metadata conventions. The files can be accessed and processed using standard scientific computing libraries such as `xarray` or `netCDF4` in Python, `ncdf4` in R, or GIS software capable of handling NetCDF raster data (e.g., QGIS, ArcGIS).

Each NetCDF file contains a three-dimensional data array (time, latitude, longitude), with daily temporal resolution and consistent grid geometry across the 1991–2020 period. Users can extract point-based time series, compute basin-averaged statistics, or perform spatial analyses directly from the gridded fields without additional pre-processing.

https://doi.org/10.5194/essd-2026-467
Preprint. Discussion started: 11 August 2026

To illustrate potential applications, daily time series can be extracted at selected grid cells and used as climatic forcing inputs for hydrological and ecohydrological models (Bancheri et al., 2018). The dataset is intended to provide spatially consistent meteorological boundary conditions rather than serving as calibration or validation observations. Its high spatial resolution enables improved representation of orographic gradients and localised climatic variability, particularly in mountainous sectors of the basin.

Gauge precipitation measurements were used as provided by the source networks without applying wind-induced undercatch corrections (Sevruk, 1989; Kochendorfer et al., 2017). This represents a known source of systematic underestimation, particularly at high-elevation stations and during snowfall events, and should be considered when applying the dataset in Alpine sectors of the basin (Adam and Lettenmaier, 2003).

Given the gridded nature of the dataset, users should consider the elevation-dependent biases identified in the Technical Validation section when applying the data in high-relief terrain. Aggregation to coarser resolutions may reduce local variability but can be appropriate for large-scale water balance studies (Montanari et al., 2013).

The length (30 years), daily temporal resolution, and spatial consistency of the dataset make it suitable for climate variability analysis, trend detection, hydrological modelling, and environmental impact assessments across the Po River District.

8 Data Records

The gridded climate dataset for the PRD is publicly available on Zenodo (Salehi et al., 2025) and is distributed under the Creative Commons Attribution 4.0 International licence (https://creativecommons.org/licenses/by/4.0/). The dataset comprises two primary products: daily precipitation and daily temperature, covering a 30-year period from January 1, 1991, to December 31, 2020. The key specifications of the dataset, including spatial resolution, temporal resolution, file format, and access information, are summarised in Table 2.

The data are organised as annual NetCDF files following Climate and Forecast (CF) conventions, with separate files for each variable and year (e.g., `precipitation_1991.nc` and `temperature_1991.nc`). Each file contains 365 (or 366) daily grids at 1 km × 1 km spatial resolution covering the entire PRD. The total archive consists of 60 NetCDF files (30 years × 2 variables).

The NetCDF format ensures compatibility with standard climate analysis tools, including Python (`xarray`, `netCDF4`), R (`ncdf4`, `terra`), and GIS software (QGIS, ArcGIS). Figure 8 illustrates both the long-term climatology and the fine-scale spatial variability of the interpolated fields, presenting the 30-year mean annual total precipitation and mean annual temperature surfaces alongside representative daily snapshots demonstrating the fine-scale variability captured across the basin's complex terrain.

https://doi.org/10.5194/essd-2026-467
Preprint. Discussion started: 11 August 2026

Table 2. Summary of gridded climate dataset specifications and access information.

Feature	Mean Daily Temperature	Daily Total Precipitation
Unit	°C	mm day^{-1}
Spatial Resolution	1 km × 1 km	1 km × 1 km
Temporal Resolution	Daily	Daily
Period	1991–2020	1991–2020
Format	NetCDF (annual files)	NetCDF (annual files)
Repository	Zenodo	Zenodo
DOI	10.5281/zenodo.19207256	
Licence	CC BY 4.0	

9 Code Availability

The kriging implementation used to generate the 1-km gridded precipitation and temperature fields is part of the GEOframe modelling system and is publicly available at https://github.com/geoframecomponents/Krigings. The model structure and implementation are described in Bancheri et al. (2018).

10 Data Availability

The gridded climate dataset for the Po River District is publicly available on Zenodo (Salehi et al., 2025) under a Creative Commons Attribution 4.0 International licence (https://creativecommons.org/licenses/by/4.0/). The DOI is https://doi.org/10.5281/zenodo.19207256.

11 Author Contribution

H.S.: Conceptualization, Methodology, Software, Formal analysis, Data curation, Writing – original draft. D.A.: Software, Writing – review & editing. S.B.: Methodology, Writing – review & editing. G.R.: Data curation, Validation, Writing – review & editing. M.B. and F.T.: Data curation. G.F.: Software, Validation, Writing – review & editing. R.R.: Conceptualization, Supervision, Validation, Writing – review & editing.

12 Competing interests

The authors declare that they have no conflict of interest.

13 Acknowledgements

355 The authors thank the regional environmental protection agencies (ARPA) for providing stations data, and the Po River Basin District Authority (ADBPO) for data access and institutional support. The EEAR-Clim dataset (Bongiovanni et al., 2025) was used to supplement boundary station coverage. The work of H.S. was funded by the Italian Space Agency (ASI) under Contract no. 2024-5-E.0, CUP Master no. I53D24000060005, SAP Fund no. 000040104905 (SpaceItUp programme). This work also received support from the 4DHydro initiative, funded by the European Space Agency (ESA) under contract 360 no. 4000141141/23/I-EF.

During the preparation of this manuscript, the authors used Claude (Anthropic) to assist with English language editing, grammar correction, and improving the clarity and readability of the text. The authors reviewed and edited all AI-assisted text and take full responsibility for the content of the manuscript. No AI tools were used to generate research data, perform analyses, or create figures or tables.

References

Aalto, J., Pirinen, P., Heikkinen, J., and Venäläinen, A.: Spatial interpolation of monthly climate data for Finland: comparing the performance of kriging and generalized additive models, Theoretical and Applied Climatology, 112, 99–111, https://doi.org/10.1007/s00704-012-0716-9, 2013.

Aalto, J., Le Roux, P. C., and Luoto, M.: The meso-scale drivers of temperature extremes in high-latitude Fennoscandia, Climate Dynamics, 42, 237–252, https://doi.org/10.1007/s00382-013-1821-x, 2014.

Abatzoglou, J. T., Dobrowski, S. Z., Parks, S. A., and Hegewisch, K. C.: TerraClimate, a high-resolution global dataset of monthly climate and climatic water balance from 1958–2015, Scientific Data, 5, 170 191, https://doi.org/10.1038/sdata.2017.191, 2018.

Adam, J. C. and Lettenmaier, D. P.: Adjustment of global gridded precipitation for systematic bias, Journal of Geophysical Research: Atmospheres, 108, https://doi.org/10.1029/2002JD002499, 2003.

Bancheri, M., Serafin, F., Bottazzi, M., Abera, W., Formetta, G., and Rigon, R.: The design, deployment, and testing of kriging models in GEOframe with SIK-0.9.8, Geoscientific Model Development, 11, 2189–2207, https://doi.org/10.5194/gmd-11-2189-2018, 2018.

Bashfield, A. and Keim, A.: Continent-wide DEM creation for the European Union, in: 34th International Symposium on Remote Sensing of the Environment, 2011.

Beck, H. E. et al.: Present and future Köppen-Geiger climate classification maps at 1-km resolution, Scientific Data, 5, 1–12, https://doi.org/10.1038/sdata.2018.214, 2018.

Bongiovanni, G. et al.: EEAR-Clim: a high-density observational dataset of daily precipitation and air temperature for the Extended European Alpine Region, Earth System Science Data, 17, 1367–1391, https://doi.org/10.5194/essd-17-1367-2025, 2025.

Bourgault, G.: Clarifications and new insights on conditional bias, Mathematical Geosciences, 53, 623–654, https://doi.org/10.1007/s11004-020-09864-7, 2021.

Copernicus Land Monitoring Service: European Digital Elevation Model (EU-DEM), European Environment Agency, https://www.eea.europa.eu/data-and-maps/data/copernicus-land-monitoring-service-eu-dem, 2016.

Cornes, R. C., van der Schrier, G., van den Besselaar, E. J. M., and Jones, P. D.: An ensemble version of the E-OBS temperature and precipitation datasets, Journal of Geophysical Research: Atmospheres, 123, 9391–9409, https://doi.org/10.1029/2017JD028200, 2018.

Daly, C. et al.: Physiographically sensitive mapping of climatological temperature and precipitation across the conterminous United States, International Journal of Climatology, 28, 2031–2064, https://doi.org/10.1002/joc.1688, 2008.

Dorninger, M., Schneider, S., and Steinacker, R.: On the interpolation of precipitation data over complex terrain, Meteorology and Atmospheric Physics, 101, 175–189, https://doi.org/10.1007/s00703-007-0285-2, 2008.

Frazier, A. G., Giambelluca, T. W., Diaz, H. F., and Needham, H. L.: Comparison of geostatistical approaches to spatially interpolate month-year rainfall for the Hawaiian Islands, International Journal of Climatology, 36, 1399–1414, https://doi.org/10.1002/joc.4437, 2016.

Frei, C. and Schär, C.: A precipitation climatology of the Alps from high-resolution rain-gauge observations, International Journal of Climatology, 18, 873–900, https://doi.org/10.1002/(SICI)1097-0088(19980630)18:8<873::AID-JOC255>3.0.CO;2-9, 1998.

Gebrechorkos, S. et al.: A high-resolution daily global dataset of statistically downscaled CMIP6 models for climate impact analyses, Scientific Data, 10, 611, https://doi.org/10.1038/s41597-023-02465-x, 2023.

Goovaerts, P.: Geostatistical approaches for incorporating elevation into the spatial interpolation of rainfall, Journal of Hydrology, 228, 113–129, https://doi.org/10.1016/S0022-1694(00)00144-X, 2000.

https://doi.org/10.5194/essd-2026-467
Preprint. Discussion started: 11 August 2026

Gupta, H. V., Kling, H., Yilmaz, K. K., and Martinez, G. F.: Decomposition of the mean squared error and NSE performance criteria: Implications for improving hydrological modelling, Journal of Hydrology, 377, 80–91, https://doi.org/10.1016/j.jhydrol.2009.08.003, 2009.

Harris, I., Osborn, T. J., Jones, P., and Lister, D.: Version 4 of the CRU TS monthly high-resolution gridded multivariate climate dataset, Scientific Data, 7, 109, https://doi.org/10.1038/s41597-020-0453-3, 2020.

Haylock, M. R. et al.: A European daily high-resolution gridded data set of surface temperature and precipitation for 1950–2006, Journal of Geophysical Research: Atmospheres, 113, D20 119, https://doi.org/10.1029/2008JD010201, 2008.

Hengl, T., Heuvelink, G. B., and Rossiter, D. G.: About regression-kriging: From equations to case studies, Computers & Geosciences, 33, 1301–1315, https://doi.org/10.1016/j.cageo.2007.05.001, 2007.

Herrera, S. et al.: Uncertainty in gridded precipitation products: Influence of station density, interpolation method and grid resolution, International Journal of Climatology, 39, 3737–3752, https://doi.org/10.1002/joc.5878, 2019.

Hijmans, R. J., Cameron, S. E., Parra, J. L., Jones, P. G., and Jarvis, A.: Very high resolution interpolated climate surfaces for global land areas, International Journal of Climatology, 25, 1965–1978, https://doi.org/10.1002/joc.1276, 2005.

Hofstra, N., New, M., and McSweeney, C.: The influence of interpolation and station network density on the distributions and trends of climate variables, Climate Dynamics, 35, 841–858, https://doi.org/10.1007/s00382-009-0645-z, 2010.

Hofstra, N. et al.: Comparison of six methods for the interpolation of daily, European climate data, Journal of Geophysical Research: Atmospheres, 113, D21 110, https://doi.org/10.1029/2008JD010100, 2008.

Isotta, F. A. et al.: The climate of daily precipitation in the Alps: development and analysis of a high-resolution grid dataset, International Journal of Climatology, 34, 1657–1675, https://doi.org/10.1002/joc.3794, 2014.

Klein Tank, A. M. et al.: Daily dataset of 20th-century surface air temperature and precipitation series for the European Climate Assessment, International Journal of Climatology, 22, 1441–1453, https://doi.org/10.1002/joc.773, 2002.

Kochendorfer, J., Rasmussen, R., Wolff, M., Baker, B., Hall, M. E., Meyers, T., Landolt, S., Jachcik, A., Isaksen, K., Brækkan, R., and Leeper, R.: The quantification and correction of wind-induced precipitation measurement errors, Hydrology and Earth System Sciences, 21, 1973–1989, https://doi.org/10.5194/hess-21-1973-2017, 2017.

Montanari, A. et al.: "Panta Rhei—everything flows": change in hydrology and society—the IAHS scientific decade 2013–2022, Hydrological Sciences Journal, 58, 1256–1275, https://doi.org/10.1080/02626667.2013.809088, 2013.

Mouratidis, A. and Ampatzidis, D.: European digital elevation model validation against extensive global navigation satellite systems data, ISPRS International Journal of Geo-Information, 8, 108, https://doi.org/10.3390/ijgi8030108, 2019.

Mouratidis, A., Briole, P., and Katsambalos, K.: SRTM 3″ DEM validation by means of extensive kinematic GPS measurements: a case study from North Greece, International Journal of Remote Sensing, 31, 6205–6222, https://doi.org/10.1080/01431160903401239, 2010.

Ntagkounakis, G., Nastos, P., Kapsomenakis, J., and Douvis, K.: Creation and comparison of high-resolution daily precipitation gridded datasets for Greece using a variety of interpolation techniques, Hydrology, 12, 31, https://doi.org/10.3390/hydrology12020031, 2025.

Ossa-Moreno, J. et al.: Comparison of approaches to interpolating climate observations in steep terrain with low-density gauging networks, Hydrology and Earth System Sciences, 23, 4763–4781, https://doi.org/10.5194/hess-23-4763-2019, 2019.

Rolland, C.: Spatial and seasonal variations of air temperature lapse rates in Alpine regions, Journal of Climate, 16, 1032–1046, https://doi.org/10.1175/1520-0442(2003)016<1032:SASVOA>2.0.CO;2, 2003.

Salamon, P. et al.: EMO: A high-resolution multi-variable gridded meteorological data set for Europe, European Commission, Joint Research Centre [Dataset], https://doi.org/10.2905/JRC.9D3F64R, 2026.

Salehi, H. et al.: A 30-Year High-Resolution (1-km) Daily Precipitation and Temperature Dataset for the Po River District (1991–2020), https://doi.org/10.5281/zenodo.19207256, dataset, 2025.

Sevruk, B.: Reliability of precipitation measurement, WMO/IAHS/ETH International Workshop on Precipitation Measurement, pp. 13–19, 1989.

Steinacker, R. et al.: A mesoscale data analysis and downscaling method over complex terrain, Monthly Weather Review, 134, 2758–2771, https://doi.org/10.1175/MWR3196.1, 2006.

Vezzoli, R., Mercogliano, P., Pecora, S., Zollo, A. L., and Cacciamani, C.: Hydrological simulation of Po River (North Italy) discharge under climate change scenarios using the RCM COSMO-CLM, Science of the Total Environment, 521, 346–358, https://doi.org/10.1016/j.scitotenv.2015.03.096, 2015.

World Meteorological Organization: Guide to Instruments and Methods of Observation, wMO-No. 8, 2018.

Zahradníček, P., Rasol, D., Cindrić, K., and Štěpánek, P.: Homogenization of monthly precipitation time series in Croatia, International Journal of Climatology, 34, 3671–3683, https://doi.org/10.1002/joc.3946, 2014.

Zanchettin, D., Traverso, P., and Tomasino, M.: Po River discharges: a preliminary analysis of a 200-year time series, Climatic Change, 89, 411–433, https://doi.org/10.1007/s10584-008-9395-z, 2008.